

Optimizing a flow-through X-ray transmission cell for studies of temporal and spatial variations of ion distributions at mineral–water interfaces

Sang Soo Lee,* Paul Fenter and Changyong Park‡

Chemical Sciences and Engineering Division, Argonne National Laboratory, 9700 South Cass Avenue, Argonne, IL 60439, USA. E-mail: sslee@anl.gov

The optimization of an X-ray transmission-cell design for high-resolution X-ray reflectivity measurements of the kinetics and thermodynamics of reactions at mineral–solution interfaces is presented. The transmission cell is equipped with a liquid flow system consisting of a pair of automated syringe pumps whose relative flow rates control the composition of a solution injected into the cell with $\sim 1\%$ precision. The reflectivity measurements from the muscovite-(001)–solution interface at photon energies of 15–16.5 keV show that the cell is useful for probing interfacial ion adsorption–desorption experiments at a time scale of several seconds or slower. The time resolution is achieved with a small-volume (~ 0.22 ml) reaction chamber to facilitate fast solution exchange. Additional reductions in reaction chamber volume will improve both the data quality by reducing X-ray absorption through the solution and the time resolution by increasing the solution exchange rate in the cell.

© 2013 International Union of Crystallography
 Printed in Singapore – all rights reserved

Keywords: X-ray transmission flow-through cell; X-ray reflectivity; crystal truncation rod; resonant anomalous X-ray reflectivity; muscovite; interfacial thermodynamics and kinetics.

1. Introduction

The fate of toxic elements and nutrients in natural aqueous environments is determined largely by their reactions with mineral surfaces (Brown *et al.*, 1999). Robust predictions on their behavior in natural environments require a fundamental understanding of the molecular-scale processes at mineral–water interfaces. High-resolution X-ray reflectivity techniques, including non-resonant crystal truncation rod (CTR) measurements (Robinson, 1986; Feidenhans'l, 1989; Fenter, 2002) and resonant anomalous X-ray reflectivity (RAXR) (Park *et al.*, 2005, 2006; Park & Fenter, 2007), are non-destructive tools that probe the interfacial structure both *in situ* and at the molecular-scale level (Als-Nielsen & McMorrow, 2001). Recent applications of these X-ray techniques on geochemical systems have provided new insights into the structures of water (Eng *et al.*, 2000; Cheng *et al.*, 2001; Schlegel *et al.*, 2002; Park *et al.*, 2004; Catalano *et al.*, 2009; Heberling *et al.*, 2011) and ions (Park *et al.*, 2006; Schlegel *et al.*, 2006; Catalano *et al.*, 2008; Fenter *et al.*, 2008; Kohli *et al.*, 2009; Lee, Fenter *et al.*, 2010) organized near various mineral surfaces. The observed distributions of ions, in particular, show the coexistence of different adsorbed species (Park *et al.*, 2006; Catalano *et al.*, 2008; Lee *et al.*, 2009) whose fractional

coverages are controlled by the hydration strength of the ions (Lee, Fenter *et al.*, 2010).

Two cell designs have been commonly used for the X-ray reflectivity experiments at liquid–solid interfaces (Fenter, 2002; Nagy & You, 2002): the ‘thin-film’ and ‘transmission’ cells (Fig. 1). The thin-film cell makes use of a capillary force between the film and the sample surface to maintain a several-micrometer-thick solution layer above the solid sample. This geometry minimizes linear attenuation of the X-ray beam

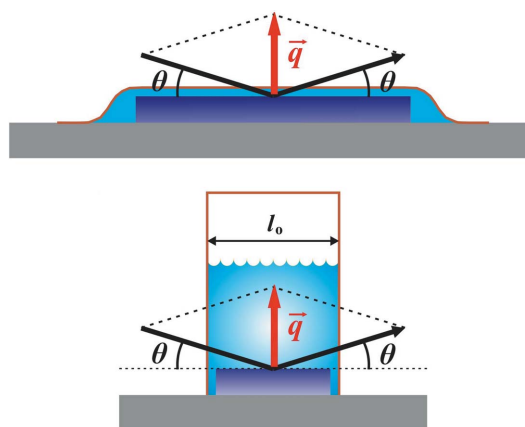


Figure 1
 Schematics of the thin-film (top) and transmission cell (bottom) designs for X-ray reflectivity experiments.

‡ Present address: HPCAT, Geophysical Laboratory, Carnegie Institution of Washington, Argonne, IL 60439, USA.

through the solution, allowing collection of data with both high quality and resolution. The transmission cell includes a several-millimeter-thick bulk solution reservoir in contact with the sample. The thick solution absorbs a large fraction of the X-ray beam, decreasing the reflectivity signal and increasing the background. Most experiments with the transmission cell have utilized a combination of small samples and relatively high photon energies in order to reduce the X-ray beam attenuation (Teng *et al.*, 2001; Fenter *et al.*, 2003, 2011).

The use of a thin-film cell for studies of reaction kinetics or thermodynamics (Park *et al.*, 2008) is difficult mainly because of three technical issues. First, the cell contains a limited amount of solution (typically ≤ 0.001 ml on a 1 cm^2 sample). Any reaction with the sample (*e.g.* dissolution) can alter the solution composition, making it difficult to measure phenomena that are sensitive to the precise solution conditions, *e.g.* determining the adsorption free energy of an ion on a mineral surface. Second, we have observed that the ion concentration within the thin water layer can increase with time even in the absence of interfacial reactions (Lee *et al.*, 2012). The effect is most significant near the center of the sample surface (Fig. 2). It is speculated that this phenomenon

is likely to be due to the diffusion of water through the permeable Kapton film (Sacher & Susko, 1979; Bellucci & Nicodemo, 1993) which leads to microscopic solution flow within the thin solution layer (from the edges to the central region of the sample). In our own measurements with a thin-film cell, X-ray reflectivity data are usually collected with the X-ray beam situated towards the sample edge and/or with frequent refreshments of the solution in the cell to minimize this effect (Lee *et al.*, 2012). Third, the formation of a stable thin solution film between the sample and the Kapton film requires a relaxation period (typically several to a few tens of minutes). This inevitable time delay makes it difficult to measure reaction dynamics, *e.g.* ion adsorption–desorption kinetics on mineral surfaces, which requires frequent refreshing of the solution in the cell.

The X-ray transmission cell is potentially better suited for measurements of interfacial reaction kinetics and thermodynamics, but the current design (Teng *et al.*, 2001; Fenter *et al.*, 2010) has not been well characterized in terms of accuracy of controlling the solution composition and rate of solution exchange. Here we present a revised design of the transmission cell developed for measuring *in situ* CTR and RAXR to investigate ion adsorption–desorption processes at the muscovite-(001)–aqueous-solution interface. This cell allows almost all aspects of ion adsorption phenomena of interest, including structure, thermodynamics and kinetics, to be observed under environments where the solution composition and flow rates are controlled dynamically. The applicability and limitations of the cell design are explored through various *ex situ* performance tests and *in situ* CTR and RAXR measurements.

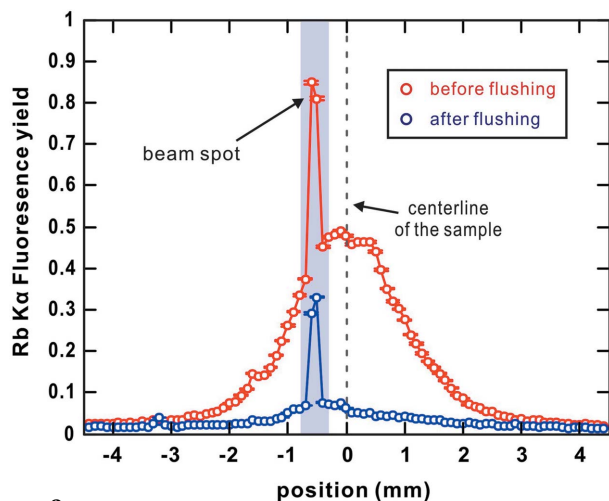


Figure 2 The spatial variation in Rb $K\alpha$ fluorescence yield (FY) from a sample mounted in an X-ray thin-film cell. The FY is plotted as a function of distance from the sample center transverse to the vertical scattering plane. The cell contained a 0.1 mM RbOH solution several micrometers in thickness. The data (‘before flushing’) were collected three hours after solution injection and subsequent reduction of the solution thickness to several micrometers. The large enhancement in FY near the center portion of the sample indicates an increase in Rb concentration. An additional FY enhancement is observed at the beam spot location (-0.7 mm) used for data acquisition for 3 h. This enhancement is due to X-ray-induced damage of the Kapton film leading to Rb incorporation (Lee *et al.*, 2012). Expanding the thin water layer and flushing several milliliters of the same solution (‘after flushing’) effectively reduced the ion-accumulation near the sample center (this did not fully remove the Rb accumulated under the beam spot). The solid sample was a 10 Å-thick TiO_2 layer coated on a Si/Mo multilayer grown by atomic layer deposition (Kohli *et al.*, 2010), with the exposed surface in dimensions of 12 mm \times 37 mm (transverse and parallel to the scattering plane, respectively). The data were collected at beamline 6-ID-B (Advanced Photon Source). The incident beam was collimated by slits to a size of 0.05 mm (v) \times 1.0 mm (h) with an incident angle of 0.275° (with a 10.5 mm beam footprint on the sample) at a photon energy of 17 keV.

2. Cell design and performance test

2.1. Cell parts

A new X-ray transmission cell equipped with an automated liquid flow system was constructed for this study. The basic framework of the cell originates from the previous transmission-cell design (Fenter, 2002). The cell body is a Teflon block of dimensions 70 mm (vertical) \times 70 mm (horizontal) \times 15 mm (thickness) (Fig. 3 and Fig. S1 of the supplementary information¹). The central part (50 mm \times 50 mm) thinned to a 3 mm-thick slab has a rectangular-shaped opening (3 mm \times 25 mm \times 3 mm) which is used as a solution reservoir. The volume of the chamber is ~ 0.22 ml (without sample), substantially smaller than the volume of the previous generation transmission cell (~ 1.2 ml).

Upon mounting a sample (in this case a muscovite single crystal; see §3.1 for the sample description) in the cell, the cell body is sealed with Kapton films (~ 0.1 mm thick) as X-ray windows, which are clamped between two metal flanges (Fig. 3b). Each metal block is a 3 mm-thick steel disk, 50 mm in diameter, with a 5.6 mm (v) \times 24 mm (h) aperture. The

¹ Supplementary data for this paper are available from the IUCr electronic archives (Reference: VV5050). Services for accessing these data are described at the back of the journal.

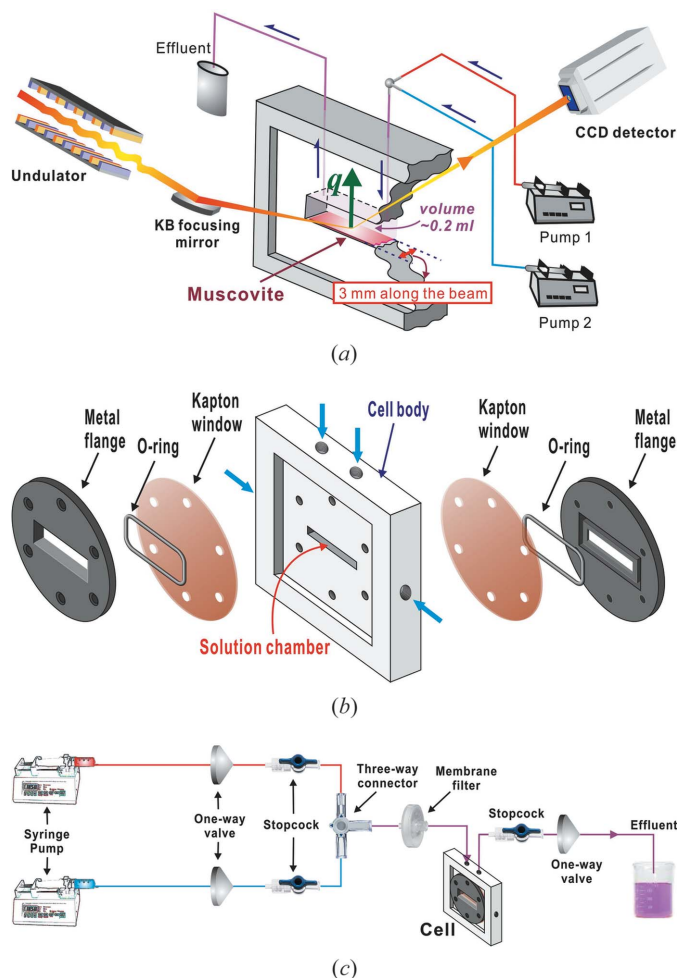


Figure 3

(a) Schematic of measuring specular X-ray reflectivity using a new flow-through transmission cell. (b) Expanded view of the assembled cell body. The cyan arrows indicate four solution exchange ports. (c) Layout of the liquid flow system.

edges of the openings are tapered ($\sim 45^\circ$) to avoid blocking the X-ray beam during scattering measurements at large incident (or exit) angles. The inner part of the block, which is in contact with the Kapton film, has a rectangular groove [1.2 mm (v) \times 3.0 mm (h)] in which an O-ring is placed to seal the cell.

The Teflon cell body has four ports through which solution can be injected into or dispensed from the chamber (Fig. 3b). The hole diameter ($\sim 80 \mu\text{m}$) is chosen to minimize the cell volume but large enough to allow unrestricted flow. These ports are accessed by threaded holes (1/4–28) to connect to the liquid flow system. Two of these ports are on the top of the cell body and the other two ports are on the sides of the body (Fig. 3b). Injection of a solution from the top of the cell appears to improve the solution mixing in the cell by reducing the tendency to form lamellar flow conditions above the sample surface (see §3.4.2 for details). Furthermore, air bubbles, which can form during experiments, tend to accumulate in the top part of the chamber, and are more easily removed when the outflow goes through the ports in the chamber ceiling.

2.2. Liquid flow system

The flow system is designed to have the capability of handling multiple sources of liquids in different chemical compositions. It has a computer-controlled pump system which can vary the liquid flow rate (from 0.05 ml to 20 ml per minute) to simulate the timescales for solution exchange measurements. The solution composition in the chamber can be controlled by changing the relative flow rates of the multiple end-member solutions. For example, the Rb/Na concentration in the mixed solution can be tuned by controlling the flow rates of $1 \times 10^{-2} \text{ M}$ RbCl and $1 \times 10^{-2} \text{ M}$ NaCl solutions (M : molarity) without changing the ionic strength (and Cl^- concentration). This feature is useful particularly for adsorption isotherm measurements where solution composition needs to be tuned by small compositional steps.

The current system makes use of a pair of syringe pumps (AL-1000; World Precision Instruments), each of which controls the flow rate with a volumetric precision of $\sim 0.3 \mu\text{l}$ when using a 50 ml syringe (or a translational precision of $\sim 0.5 \mu\text{m}$). The maximum flow rate using a 50 ml syringe is $\sim 28 \text{ ml min}^{-1}$, but it can be increased, if needed, by using multiple pumps containing the same solution. The use of multiple pumps also allows fine adjustments of the solution composition in the cell by changing the mixing ratio of two (or more) end-member solutions with different compositions (see §2.3.2 for details). The pumps are operated using customized Matlab-based software (which can control up to 100 pumps simultaneously). A syringe (typically 50 ml in volume) containing an experimental solution is mounted to each pump and connected to a polypropylene tube (1.2 m long). A one-way ('check') valve is used to prevent solution back-flow (*i.e.* from the transmission cell to the fluid source) (Fig. 3c). Each check valve is attached to one of two stop valves, which are linked to a three-way connector coupled with a membrane filter with a nominal average pore size of $0.45 \mu\text{m}$. The filter (in combination with injecting the solution from the top of the cell) is required to mix effectively the solutions at fast flow rates (see §3.4.2). A one-way valve and a stop valve are also placed in the cell outlet to prevent a reverse flow (*i.e.* from effluent reservoir into the cell). The effluent reservoir is placed at a higher elevation than the cell body to prevent a spontaneous discharge of a solution from the cell by gravity.

2.3. Performance test

2.3.1. Basic calculations for X-ray measurements. During X-ray reflectivity measurements the absorption of X-rays by the solution decreases the reflected signal and increases the background, making X-ray measurements more challenging (see §3.2 for comparison of X-ray data measured in the current cell with those measured in a thin-film cell). X-ray transmission through water (T) is calculated without considering absorption by solutes [see equation (7) for the element-specific absorption effect] as

$$T = I/I_0 = \exp(-l/\Lambda_w), \quad (1)$$

Table 1

Calculated q ranges for specular X-ray reflectivity measurements using an X-ray transmission flow-through cell utilized in this study.

q_{\min} and q_{\max} : minimum and maximum q values, respectively, calculated based on a sample length of 3 mm and a vertical beam size of 50 μm .

	Energy (keV)				
	10	15	20	30	50
q_{\min} (\AA^{-1})	0.17	0.25	0.34	0.51	0.84
q_{\max} (\AA^{-1})	9.0	13.6	18.1	27.1	45.2

where l is the X-ray path length through the solution and Λ_w is the X-ray attenuation length of water. The transmission factor becomes smaller with decreasing photon energy because of the decrease in Λ_w . For example, the calculated transmission of X-rays through 3 mm-thick water is $\sim 20\%$ at 10 keV ($\Lambda_w \simeq 2$ mm) compared with $\sim 80\%$ at 20 keV ($\Lambda_w \simeq 14$ mm) (Fig. 4). The transmission also decreases with increasing incident and/or exit angles of X-rays to the sample (Fig. 4). At the specular reflection condition the path length through the solution is inversely proportional to the cosine of the incident angle, θ , $l = l_0/\cos\theta$, where l_0 is the cell thickness along the beam direction. The path length can also be expressed as $l_0/[1 - (\hbar c q/2E)^2]^{1/2}$ when written as a function of vertical momentum transfer $q = 4\pi\sin\theta/\lambda$, where λ is the X-ray wavelength, E is the X-ray photon energy and $\hbar c = 1973$ eV \AA .

The sample length along the beam direction, d , determines the lowest angle of incidence, θ_{\min} , at which a sample can fully accept the X-ray beam for a given vertical beam size, Δ , without the beam footprint exceeding the sample size (*i.e.* ‘spill-off’). For the specular reflection condition, $\theta_{\min} \simeq 1^\circ$ for $d = 3$ mm and $\Delta = 50$ μm . This angle corresponds to the

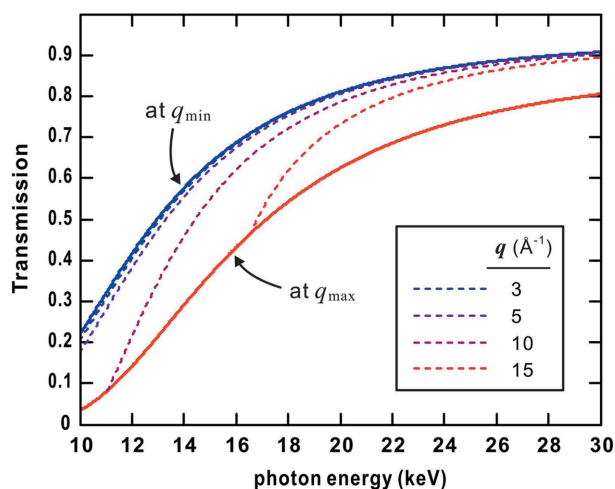


Figure 4

Calculated X-ray transmission through an X-ray transmission cell containing 3 mm-thick water as a function of photon energy. The values are calculated for different momentum transfer (q) conditions. q_{\min} and q_{\max} are the minimum and maximum q values, respectively, to which specular X-ray reflectivity data can be measured using a current transmission cell (see Table 1), calculated based on the sample length (for q_{\min}) and the vertical cell opening (for q_{\max}).

Table 2

Solution mixing experiments.

$f_{\text{mix,calc}}$: volumetric mixing ratio (*i.e.* volume of the pH 2 solution over that of the pH 4 solution) calculated based on the flow rates. pH_{calc} : pH of the mixed solution calculated based on $f_{\text{mix,calc}}$. pH_{meas} : measured pH of the mixed solution. Measurements were duplicated and the mean values are reported. $f_{\text{mix,meas}}$: measured mixing ratio calculated based on pH_{meas} .

Sample	Flow rate (ml min^{-1})		$f_{\text{mix,calc}}$	pH_{calc}	pH_{meas}			$f_{\text{mix,meas}}$
	pH 2 \dagger	pH 4 \dagger			A	B	Mean	
Set 1	0.00	3.00	0.00	4.09	3.81	3.87	3.84 \ddagger	0.006 \ddagger
Set 2	0.03	2.97	0.01	3.71	3.71	3.71	3.71	0.010
Set 3	0.30	2.70	0.10	2.91	2.93	2.95	2.94	0.094
Set 4	0.90	2.10	0.30	2.46	2.46	2.47	2.47	0.294
Set 5	1.50	1.50	0.50	2.24	2.24	2.24	2.24	0.500

\dagger Nominal pH; measured values were 1.94 and 4.09, respectively. \ddagger The difference between hydronium concentrations of the measured and calculated solutions for Set 1 is $|10^{-3.84} - 10^{-4.09}| = 6.33 \times 10^{-5}$, which is 0.6% of the difference between those of two end-member solutions $|10^{-1.94} - 10^{-4.09}| = 1.14 \times 10^{-2}$.

minimum vertical momentum transfer, $q_{\min} [= 4\pi\sin(\theta_{\min})/\lambda]$, ranging from 0.17 to 0.34 \AA^{-1} , for the photon energies from 10 to 20 keV, respectively (Table 1). This q_{\min} range is similar to that of X-ray reflectivity measurements at the mineral–water interface in thin-film cell geometry using an unfocused beam in sizes of ≥ 100 μm (Fenter, 2002). Reflectivity measurements also can be performed at $q \leq q_{\min}$, especially at higher photon energies where the q_{\min} values are relatively large (Table 1), with the inclusion of an additional correction for X-ray beam spill-off from the sample surface.

The vertical dimension of the sample chamber determines the largest incident and exit angles that can be reached in the X-ray measurements. This is an important design criterion because the maximum q value (q_{\max}) defines the spatial resolution ($= \pi/q_{\max}$) of X-ray reflectivity data (Fenter & Sturchio, 2004). The height of the chamber in the current cell is 3 mm, corresponding to the maximum angle of $\sim 60^\circ$, which is large enough for measurements of X-ray reflectivity data with a sub-angstrom scale resolution at ≥ 10 keV (Table 1).

2.3.2. Test of the precision of solution mixing. One of the aims of developing the current cell is to have the capability of measuring thermodynamically controlled properties at a mineral–solution interface. Mixing of solutions using multiple pumps enables us to produce a series of solutions with varying compositions dynamically without the need to prepare individual solutions separately. This feature also allows us to control the solution composition in the cell on a finer scale, making it possible to determine thermodynamic quantities, such as adsorption free energies, more accurately.

We first tested the precision of the current cell system for controlling the composition of mixed solutions (Table 2). Two solutions at nominal pH of 2 and 4 were prepared using a 0.01 M HCl stock solution. The measured pH values of the solutions were 1.94 and 4.09 determined with a typical 1σ uncertainty of 0.03 pH units of the pH electrode. The solutions were injected into the cell by using two syringe pumps with varying the ratio between the flow rates of the pumps. The sum of the flow rates was set to 3 ml min^{-1} . For each experiment about 3 ml of the mixed solution was collected for the pH measurement after the exchange of the solutions for several

minutes. Five combinations of different flow rates were tested, and each measurement was duplicated.

The measured mixing ratios of the resultant solutions agree with those calculated on the basis of the nominal flow rate settings (Table 2). The results show that the solution composition is controlled to within 1% of the desired value for all measurements (*i.e.* the difference between the measured and calculated hydronium concentrations was smaller than 1% of those of two end-member solutions). The slight differences may be due to the residue of the previous solution in the cell chamber and/or the diffusion of solutions through the membrane in the one-way valves. The former effect can be minimized by increasing the volume of an exchanging solution (see the next section), for example by increasing the overall flow rate at the beginning of injecting a new solution. The latter effect can be reduced by continuously adding the new solution into the chamber or by mechanically blocking the flow path (*e.g.* using the stop valve).

2.3.3. Cell volume exchange rate. We investigated the relationship between the flow rate of an injected solution and the solution exchange rate in the cell chamber. The experiments were conducted using deionized water (transparent) and a black solution (prepared by diluting carbon black pigment dispersed in a 2:1 mixture of ethanol and 2-propanol with deionized water by a factor of ~ 100). The chamber was filled initially with the black carbon solution, and deionized water was injected into the cell while the transmission of visible light through the solution in the chamber was monitored (Fig. 5*a*) (a transparent polypropylene film was used as the window material for these measurements). Thirteen exchange experiments were conducted with different flow rates (ranging from 0.25 to 9 ml min⁻¹), and six of them were duplicated. The measured data were fit to an exponential decay function as

$$T(t) = \begin{cases} T_{\min}, & t < 0, \\ [1 - \exp(-t/\tau)](T_{\max} - T_{\min}), & t \geq 0, \end{cases} \quad (2)$$

where $T(t)$ is the measured transmission as a function of time t (s) after the injection of deionized water into the chamber ($t = 0$), T_{\max} and T_{\min} are maximum and minimum transmission values (*i.e.* through transparent deionized water and the black carbon solution, respectively), and τ is the decay constant (s) for the exchange reaction.

We quantify the relationship between the flow rate and the time needed to exchange 50% of the solution in the cell, $t_{1/2} = \tau \log 2$, calculated using the τ values derived from the best fits to all exchange experiments at different flow rates. The result shows that $t_{1/2}$ is inversely proportional to the flow rate (Q) of the injected solution (Fig. 5*b*) as

$$t_{1/2} = (22 \pm 2)/Q. \quad (3)$$

This relationship indicates that the solution exchange is controlled by the volume of solution injected into the chamber. This result reveals that 50% of the solution is exchanged for every 0.36 ± 0.03 ml of injected solution (*i.e.* $t_{1/2}$ [s] $\times Q$ [ml min⁻¹]/60), which is $\sim 60\%$ larger than the

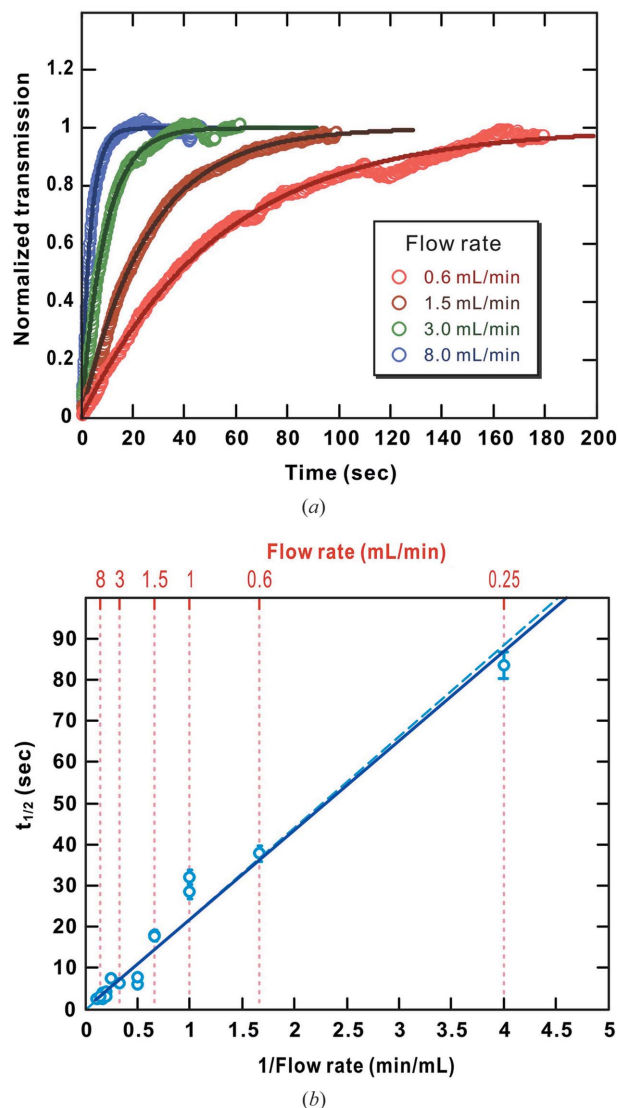


Figure 5

(*a*) Temporal changes in the transmission of visible light through the transmission cell as a function of time during the solution exchange (from the dyed solution to deionized water) in the cell. Normalized transmission is defined as $T(t)/(T_{\max} - T_{\min})$, where $T(t)$ is the measured transmission as a function of time, t (*i.e.* $t = 0$ when deionized water was injected), and T_{\max} and T_{\min} are maximum and minimum transmission values (*i.e.* through deionized water and the dyed solution), respectively. Four data sets are plotted for different flow settings (from 0.6 to 8 ml min⁻¹). (*b*) Relationship between the observed exchange time, $t_{1/2}$, and the inverse flow rate. The exchange time, $t_{1/2}$, is defined by the relation $T(t_{1/2}) = (T_{\max} - T_{\min})/2$, and calculated based on the best fit to the data using equation (2). The solid blue line represents the best fit through the data using equation (3). The data were also fit to a model without the 0.25 ml min⁻¹ data (dashed cyan line) to confirm that the slope parameter is not controlled by one outlier.

chamber volume (~ 0.22 ml). The result also shows that the exchange time is defined solely by the flow rate (Fig. 5*b*). The current cell allows for measurements of the reaction kinetics occurring in the time scale of several seconds or slower when the flow rate of ≤ 10 ml min⁻¹ is used.

To optimize the kinetics while minimizing the volume of solution that is used for the measurements, we have developed a strategy of ‘fast exchange’ and ‘steady flow’. The initial fast-

exchange stage uses a relatively high flow rate. For example, $t_{1/2}$ is ~ 2.4 s with a 9 ml min^{-1} flow rate. The solution in the cell will be fully exchanged to $>99\%$ of the desired concentration after injection of ~ 11 cell volumes [= $(0.36/0.22) \times \log(0.01/\log(0.5))$], or ~ 27 s with the 9 ml min^{-1} flow rate, after which the flow rate can be decreased to a slower rate (e.g. 1 ml min^{-1}) for the steady-flow stage.

3. Experimental results

3.1. Setting for X-ray reflectivity measurements

The applicability of the current cell for X-ray reflectivity experiments was tested by measuring the data from the (001) plane of muscovite mounted in the cell. Muscovite mica, $\text{K}_2\text{Al}_4(\text{Si}_6\text{Al}_2)\text{O}_{20}(\text{OH})_4$ (Bailey, 1984), is one of the most abundant rock-forming minerals. This phyllosilicate mineral has a tetrahedral–octahedral–tetrahedral layer structure with K^+ in the interlayer. Its (001) plane is a perfect cleavage plane and has been widely investigated as an analogue of major surfaces of clay minerals (Pashley, 1982; Israelachvili & Pashley, 1983; Israelachvili & Wennerström, 1996; Sposito *et al.*, 1999; Park *et al.*, 2006; Schlegel *et al.*, 2006; Bowers *et al.*, 2008; Lee, Fenter *et al.*, 2010; Loh & Jarvis, 2010; Lee *et al.*, 2011).

Single crystals of muscovite were prepared by slicing a larger crystal ($25 \text{ mm} \times 25 \text{ mm} \times 0.15 \text{ mm}$) into ~ 2.5 mm-wide slabs. This mechanical cutting can lead to distortions of the crystal (e.g. mosaicity), which increases the difficulty of X-ray reflectivity measurements (see §3.2). The fresh (001) plane of the crystal was exposed by cleaving with tape and rinsed with deionized water (Park *et al.*, 2008). The wet crystal was placed in the chamber and held firmly by two small Teflon cubes (about 3 mm long in each side) placed at each end of the crystal (*i.e.* no glue was used for the sample mounting.) The presence of the sample and the Teflon blocks reduces the cell volume to 0.17 ml (compared with 0.22 ml without them). The cell assemblage was completed by following the sequence described in §2.1. The sample was kept wet in the assembly process.

The X-ray measurements were conducted at beamlines 6-ID-B and 33-ID-D at the Advanced Photon Source. At 6-ID-B the monochromatic undulator beam was collimated to $0.2 \text{ mm (v)} \times 0.5 \text{ mm (h)}$ using slits and then was vertically focused by a Kirkpatrick–Baez mirror. The focused beam had a vertical size of about $30 \mu\text{m}$ at the sample position with a flux of $\sim 10^{12}$ photons s^{-1} . At 33-ID-D the beam was focused using a toroidally bent beamline mirror, and then collimated with slits [$50 \mu\text{m (v)} \times 0.5 \text{ mm (h)}$] to maintain a beam flux of $\sim 10^{11}$ photons s^{-1} .

Detailed descriptions of X-ray reflectivity techniques are shown elsewhere (Fenter, 2002; Park & Fenter, 2007). All X-ray measurements were conducted at the specular reflection condition (*i.e.* incident angle = exit angle). The incident and reflected beam fluxes were counted using an ionization chamber and a charge-coupled-device (CCD) X-ray detector (Fenter *et al.*, 2006), respectively.

3.2. CTR measurements

The X-ray reflectivity signal, $R(q, E)$, is the ratio of the reflected to incident X-ray photon flux and is defined as

$$R(q, E) = T(q, E)B(q)(4\pi r_e/A_{\text{UC}})^2(1/q)^2|F(q, E)|^2, \quad (4)$$

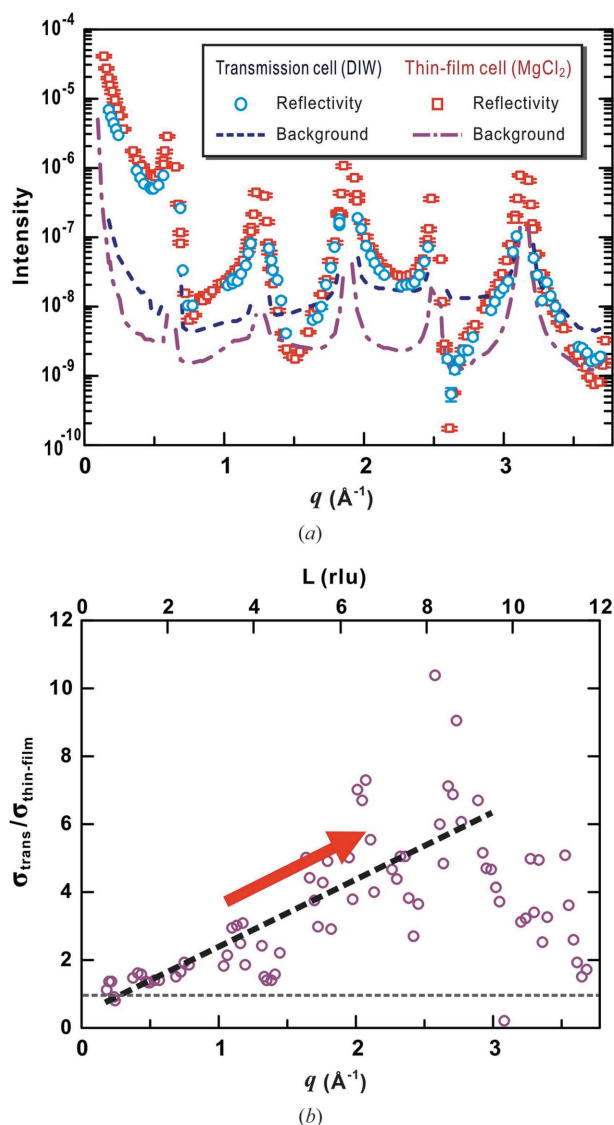
where $T(q, E)$ is the X-ray transmission through the cell [equation (1)], $B(q)$ is the roughness factor (Robinson, 1986; Fenter, 2002), r_e is the radius of an electron, and A_{UC} is the unit-cell area on the (001) plane ($= 46.72 \text{ \AA}^2$) (Schlegel *et al.*, 2006). $F(q) = F_{\text{NR}}(q) + F_{\text{R}}(q, E)$ is the structure factor of the interface including the non-resonant (NR) and resonant (R) contributions (the latter of which will be discussed in §3.3 in the context of RAXR measurements). The non-resonant structure factor is defined as

$$F_{\text{NR}}(q) = \sum_j f_j^o(q) \int \rho_j(z) \exp(iqz) dz, \quad (5)$$

where f_j^o is the form factor of an atom j and $\rho_j(z)$ is the density profile of the atom as a function of distance (z) from a reference plane (e.g. the muscovite–solution interface). The q -dependent X-ray transmission function, $T(q, E)$, is controlled by the length of the beam path through the sample cell [equation (1)]. The attenuation of the beam by solution is typically larger for the transmission cell than the thin-film cell, except at extremely small incident angles. The reduction of the X-ray beam intensity by the solution leads to an increase in the diffuse (background) intensity, decreasing the signal-to-background ratio. Both $B(q)$ and $F_{\text{NR}}(q)$ values are controlled by the interfacial structure, and are independent of the type of cell.

The specular CTR data from the muscovite (001)–water interface using the transmission cell were collected at 6-ID-B at a photon energy of 16 keV and with q ranging from 0.2 to 3.7 \AA^{-1} corresponding to Bragg index L ranging from 0.6 to 11.7 reciprocal lattice units (r.l.u.) [$q = (2\pi/d_{001})L$, where $d_{001} \simeq 19.96 \text{ \AA}$ (Schlegel *et al.*, 2006) is the lattice spacing perpendicular to the muscovite (001) plane] (Fig. 6a). For this muscovite sample the reflected images were more widely spread along the q direction because of the higher mosaicity of the crystal compared with those normally used in the thin-film cell experiments. This increase in mosaicity is presumably due to the distortion of the sample during the preparation (§3.1). The precise quantification of the reflectivity close to the Bragg conditions [*i.e.* $|q - q_{\text{Bragg}}| \leq 0.05 \text{ \AA}^{-1}$ where $q_{\text{Bragg}} = (2\pi/d_{001})L$ when L is an even number] was not possible because the reflected images overlapped with the strongly non-linear background variation associated with a tail of Bragg peaks whose intensities are typically much larger than the surface signals. The sample also showed the significant intensity at forbidden Bragg peaks along the specular truncation rod (*i.e.* at $L = 1, 3, 5, \dots$) caused by crystal defects.

The measured data are compared with those obtained using a thin-film cell (Cheng *et al.*, 2001; Fenter, 2002; Schlegel *et al.*, 2006; Lee *et al.*, 2007). The experimental details for the thin-film cell measurements were unchanged from those for the transmission-cell measurements (see §3.1 for details) except that those data were measured with a larger muscovite crystal


Figure 6

(a) Crystal truncation rod data from the muscovite-(001)–solution interface measured using a transmission flow-through cell (cyan circles) in comparison with that using a thin-film cell (red squares). The background intensity of these two data are also plotted for comparison. Both data were measured at beamline 6-ID-B with the same experimental setting but with different solution conditions. The transmission-cell data were measured in deionized water at 353 K (labeled as DIW) and the thin-film cell data were in a $1 \times 10^{-4} \text{ M}$ MgCl_2 solution at 298 K (labeled as MgCl_2). (b) Ratio of the fractional uncertainty (*i.e.* = uncertainty/signal) of the transmission-cell data (σ_{trans}) to that of the thin-film cell data ($\sigma_{\text{thin-film}}$), as a function of momentum transfer, q . The q -dependent increase of the ratio at $q \leq 2.7 \text{\AA}^{-1}$, indicated by the red arrow, is mainly due to the increased background intensity for the transmission-cell data. The ratio decreases at higher q and this is mostly related to smaller background intensity [mostly diffuse scattering from water; see the background intensity variation in (a)] and also larger reflectivity for the transmission-cell data compared with the thin-film cell data (note that these data were measured under different solution conditions).

(25 mm \times 25 mm \times 0.15 mm) in contact with a $1 \times 10^{-4} \text{ M}$ MgCl_2 solution and at a photon energy of 14 keV. The two reflectivity datasets are qualitatively similar (Fig. 6) but the overall reflectivity intensities measured in the transmission cell are $\sim 30\%$ lower than those in the thin-film cell because of

X-ray absorption by solution (Fig. 4). Additional loss of the reflectivity is observed at low q ($\leq 0.32 \text{\AA}^{-1}$ or $L \leq 1 \text{ r.l.u.}$) presumably because of beam spill-off (which was expected to be significant for $q \leq 0.32 \text{\AA}^{-1}$, based on the beam and sample sizes). The differences in the reflectivity at L between 10 and 12 r.l.u. are likely related to differences in the intrinsic interfacial structure between the two solutions.

Overall, the reflectivity data measured in the transmission cell have a quality and q -range suitable for the full structure analysis with atomic scale resolution. It is nevertheless more challenging to collect the same quality data (*i.e.* with the same precision and resolution) using the transmission cell as the data using the thin-film cell. The difference in data quality is illustrated by the mean fractional uncertainty of the measured data in the transmission cell (Fig. 6b), which is systematically larger than that measured in the thin-film cell despite the ~ 2.5 -fold longer measurement time. Note in particular that the ratio of signal uncertainties, $\sigma_{\text{trans}}/\sigma_{\text{thin-film}}$, increases with q , ranging in value from ~ 1 at very small q (where the signal-to-background intensity ratio is high, *i.e.* ≥ 100) to ~ 6 near $q = 2.7 \text{\AA}^{-1}$. The main factor that leads to this larger uncertainty in the data (even with an increased data collection time) is the higher background level for the transmission-cell data (Fig. 6a). The background intensity is mostly from X-rays scattered by the solution phase. It becomes larger with increasing q (Fig. 6a), because the beam path through solution increases with increasing the incident angle (or q) (Fig. 4). This effect limits the precision of CTR data where intrinsic reflectivity signals are small. For the current data the background intensities are similar to or even larger than the reflectivity signals at $q \geq 2.5 \text{\AA}^{-1}$ (corresponding to $L > 8 \text{ r.l.u.}$) except data measured near the (0 0 10) Bragg peak.

3.3. RAXR measurements

The RAXR technique utilizes the anomalous dispersion of a resonant atom to determine element-specific distributions at an interface (Park & Fenter, 2007). Each RAXR spectrum is measured as a function of photon energy (at a fixed q) near an X-ray absorption edge of a specific atom of interest. The intrinsic RAXR signal exhibits a modulation shape determined by the interference between non-resonant structure factor, F_{NR} [equation (5)], and resonant structure factor, F_{R} , expressed as

$$F_{\text{R}}(q, E) = (f' + if'') \int \rho_{\text{R}}(z) \exp(iqz) dz, \quad (6)$$

where $(f' + if'')$ and ρ_{R} are the energy-dependent anomalous dispersion factors and the interfacial density profile of the resonant atom, respectively.

An intrinsic RAXR signal is obtained by normalizing the measured spectrum to the energy-dependent linear absorption function of X-rays by water and other non-resonant elements [equation (1)] and by the resonant atom in solution. In the transmission-cell geometry the change in X-ray transmission by the absorption of the dissolved resonant element can be expressed as

$$T_{\text{RA}}(E) \cong \exp(-2 \times 10^{-23} N_a r_e \lambda c_{\text{RA}} f''l), \quad (7)$$

where $N_a = 6.02 \times 10^{23}$ atom mol⁻¹ is the Avogadro number, $r_e = 2.818 \times 10^{-5}$ Å is the classical electron radius, λ is the X-ray wavelength (Å), c_{RA} is the concentration of a resonant atom (mol l⁻¹), f'' is the imaginary part of the anomalous dispersion of the resonant atom, and l is the X-ray path length through the solution (mm). Fig. 7 illustrates the X-ray absorption spectra calculated for 3 mm-thick solutions containing various concentrations of Rb⁺ ([Rb]). At a high ion concentration (e.g. ≥ 10 mM) the magnitude of modulation, i.e. the fractional change in transmission, $\Delta T/T$, at the absorption edge of a resonant atom, becomes comparable with those of RAXR signals, which typically vary between 1 and 20% for ion adsorption measurements on the muscovite surface (Park *et al.*, 2006; Lee, Fenter *et al.*, 2010; Lee *et al.*, 2011).

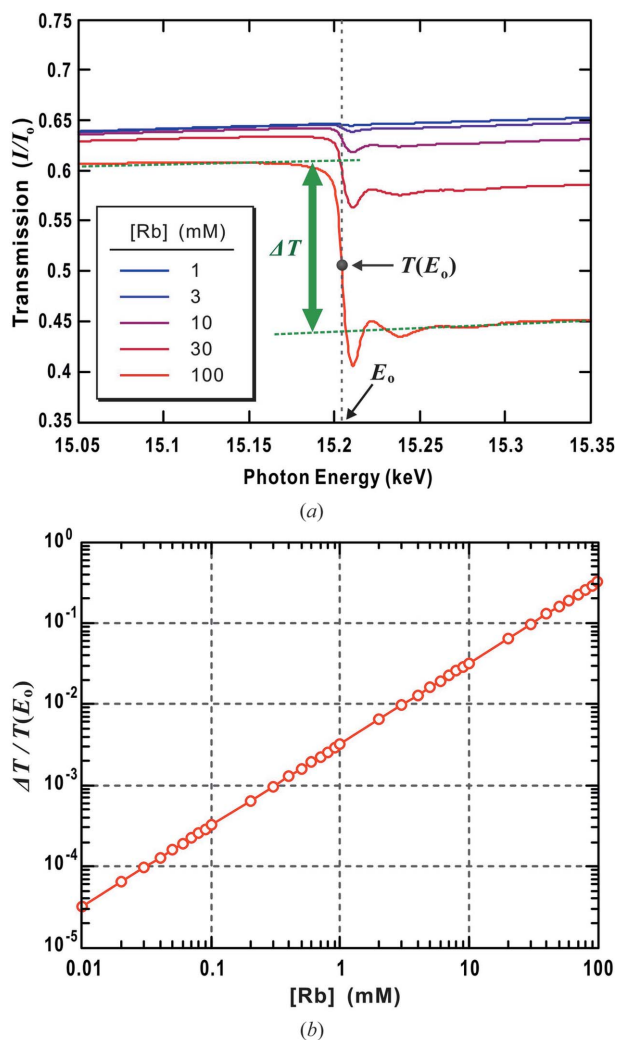


Figure 7 Energy-dependent linear absorption effect in the flow-through X-ray transmission cell. (a) Calculated X-ray absorption spectra near the Rb K-edge ($E_0 \approx 15.2$ keV) through the RbCl solutions (3 mm-thick along the beam direction) as a function of Rb concentration, [Rb]. I_0 and I indicate incident and transmitted X-ray fluxes, respectively. (b) Calculated fractional change in transmission, $\Delta T/T(E_0)$, as a function of [Rb], where $T(E_0)$ is the X-ray transmission at the Rb K-edge (E_0) and ΔT is the change in transmission at the absorption edge step.

An intrinsic RAXR signal can also be obtained by normalizing a measured spectrum to a ‘reference’ X-ray transmission spectrum, $T_{\text{ref}}(E)$, measured through a solution containing the same resonant atom in a high concentration (e.g. 0.1 M). The corrected RAXR intensity using this method is expressed as

$$R_{\text{corr}} = R_{\text{meas}} T_{\text{ref}}^{-\cos \theta (c_{\text{RA}}/c_{\text{ref}})}, \quad (8)$$

where R_{corr} and R_{meas} are the corrected and measured reflected intensities, respectively, θ is the incident angle (which is the same as the exit angle at the specular condition), and c_{RA} and c_{ref} are the concentrations of the resonant atom in a given experimental solution and a reference solution (through which the reference absorption spectrum is measured), respectively.

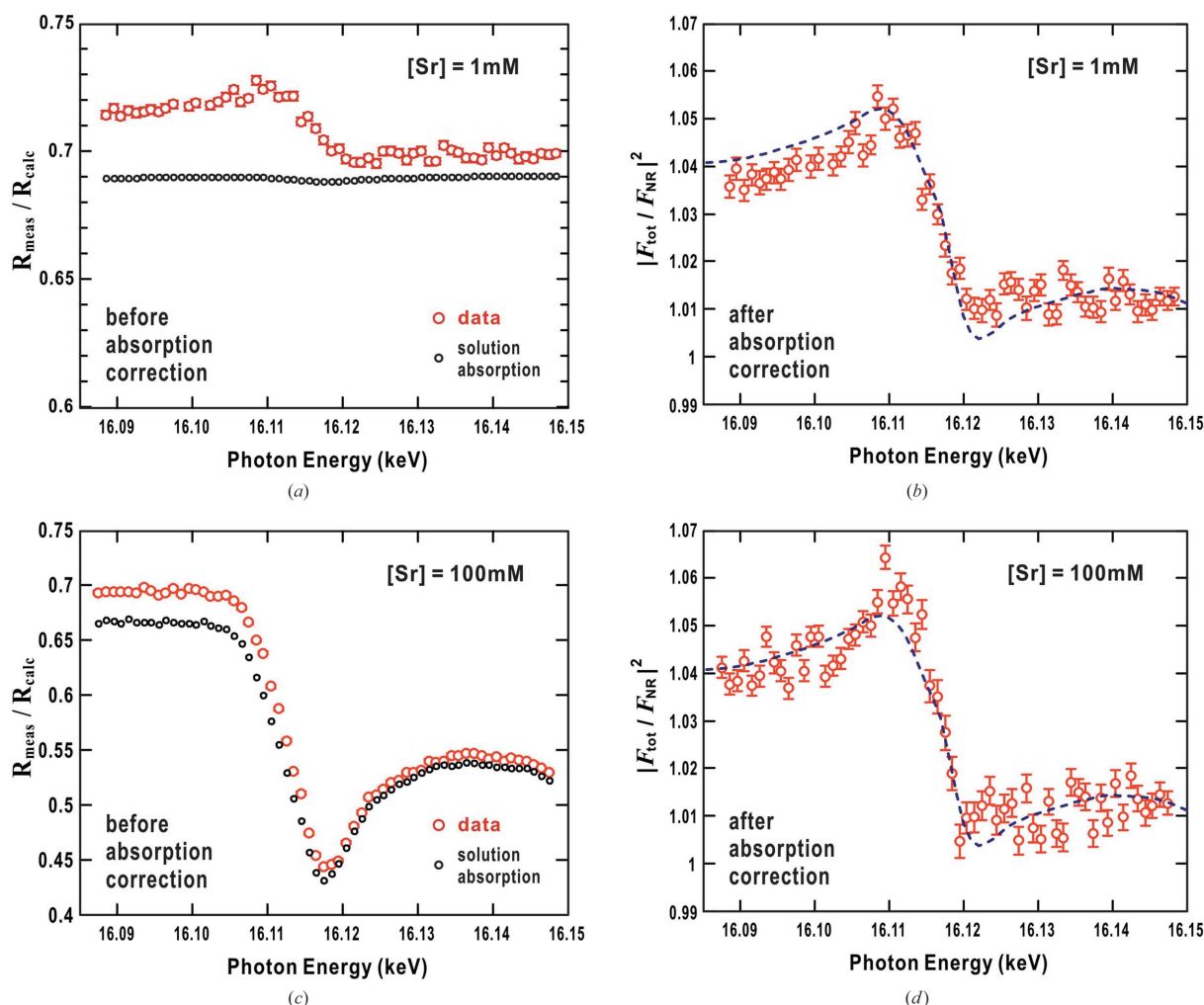
The aforementioned normalization approaches were applied to extract the intrinsic RAXR spectra from those measured from the muscovite (001) surface in 1 mM and 100 mM SrCl₂ solutions near the Sr K-edge at $q = 0.5$ Å⁻¹ (or $L = 1.6$ r.l.u.). Previous measurements suggest that the interfacial structure, i.e. adsorbed cation coverage and speciation, for these two conditions would be essentially unchanged (Park *et al.*, 2008). The spectrum measured from the 1 mM solution is similar to that previously measured in a thin-film cell (Park *et al.*, 2006), because the linear absorption by Sr ions in the solution is relatively small [Figs. 8(a) and 8(b)]. The spectrum measured from the 100 mM solution, however, is significantly different from that measured in the 1 mM solution (Fig. 8c).

The corrected reflectivity signals [Figs. 8(b) and 8(d)] were obtained using the reference absorption spectrum measured in transmission mode through the 100 mM SrCl₂ solution in the cell [equation (7)]. Both spectra are *qualitatively* similar to that previously measured in a thin-film cell (Park *et al.*, 2006), indicating that transmission-cell RAXR measurements, in principle, can be conducted even at high ion concentrations where the measured spectra include strong energy-dependent absorption by the solution species. Particular care should be taken for correcting data with small *intrinsic* RAXR signals because the precision of the data will be limited by the uncertainty of the attenuation correction (e.g. uncertainties in solution thickness or ion concentration).

3.4. Exchange experiments

The rates of the adsorption–desorption processes at a mineral–solution interface can be probed by monitoring temporal variations in reflected intensity during the solution exchange. In practice, various factors need to be considered to determine the optimal scattering condition for each data set, including the X-ray beam flux, the reflectivity magnitude at the chosen scattering condition, and the fractional change in signal strength between end-member structures. The specific momentum transfer, q , and photon energy, E , can be chosen to maximize the sensitivity to the temporal changes between two solution conditions where the interfacial structures are known.

3.4.1. Theoretical considerations. The temporal change in reflectivity can be resolved when the intrinsic fractional


Figure 8

Sr RAXR spectra measured using a flow-through transmission cell containing 1 mM and 100 mM SrCl₂ solutions [(a) and (c), respectively], at $q = 0.5 \text{ \AA}^{-1}$ ($L = 1.6 \text{ r.l.u.}$). The measured reflectivity (R_{meas}) is normalized to the non-resonant reflectivity calculated using the best-fit model to the CTR data determined previously (Park *et al.*, 2006; Lee, Park *et al.*, 2010) (R_{calc}), without considering linear absorption by solution species or resonant effects by Sr at the interface. The calculated and measured X-ray absorption spectra through the 1 mM and 100 mM solutions, respectively, are also plotted for comparison. The spectra after correction for the solution absorption are shown in (b) and (d), respectively, and are compared with that calculated based on the best-fit model of the RAXR data measured previously using a thin-film cell (Park *et al.*, 2006; Lee, Park *et al.*, 2010) (short-dashed line). The data are plotted using a non-resonant amplitude normalization (Park & Fenter, 2007) ($= |F_{\text{tot}}/F_{\text{NR}}|^2$, where F_{tot} and F_{NR} are the total and non-resonant structure factor, respectively).

change of the intensity, $|\Delta I/I|$, measured for a time interval, δt , is significantly larger than the fractional uncertainty of the data, σ/I . The time resolution is defined using the significance of the measurement, $Z = |\Delta I/I|/(\sigma/I)$, as

$$\delta t = (R + \zeta B)/\Phi [(\Delta I/I)^2 R^2/Z^2 - (\zeta \sigma_B)^2], \quad (9)$$

where R is the intrinsic reflectivity and B is the background intensity integrated over the solid angle corresponding to the ideally reflected beam cross section, Φ is the incident beam flux (in photons s⁻¹), and σ_B is the estimation error of the background B (see the supplementary information for details). The coefficient ζ is the ratio of the reflected image size to the intrinsic beam size ($\zeta = 1$ for an ideally reflecting surface) and accounts for the situation when the reflected beam is larger than ideal (and therefore with a lower signal-to-background ratio). The relationship shown in (9) indicates

that the ability to observe faster reactions can be achieved in a few ways, including larger fractional changes in the signal during reaction, $|\Delta I/I|$, a larger surface reflectivity signal, R , a larger beam flux, Φ , lower background, B , or smaller ζ (*i.e.* a surface with larger domains).

Fig. 9 shows the relationship between δt and $|\Delta I/I|$ calculated on the basis of the measured reflectivity and background intensities from the muscovite (001) surface, at $q = 0.49 \text{ \AA}^{-1}$ near the Rb K -edge ($\sim 15.2 \text{ keV}$), with an incident beam flux of 1×10^{12} photons s⁻¹. For an ideal muscovite surface ($\zeta = 1$), a signal change of $\sim 0.5\%$ is needed for reaction kinetics measurements with the 1 s time resolution. In reality, however, many muscovite (001) surfaces have non-zero mosaicity, and therefore a larger $|\Delta I/I|$ and a higher reflectivity-to-background-intensity ratio will be required in most cases.

The fractional change in signal strength can be enhanced by using resonant contrast as illustrated in Fig. 10 where RAXR

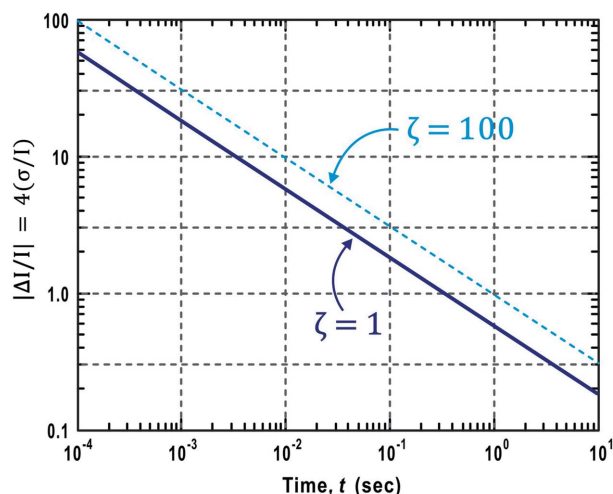


Figure 9 Relationship between the time resolution of kinetics measurements and the fractional change in signal magnitude ($|\Delta I/I|$) by changing the interfacial conditions using the flow-through transmission cell. The lines represent the significance of the measurement, $Z = |\Delta I/I|/(\sigma/I) = 4$, *i.e.* the reflectivity change is statistically significant at the 99.99% confidence interval. The values were calculated for $\Phi = 1 \times 10^{12}$ photons s^{-1} , $R = 5 \times 10^{-7}$, $B = 1 \times 10^{-8}$, corresponding to those from typical reflectivity measurements of the muscovite (001) surface using the transmission cell at $q = 0.49 \text{ \AA}^{-1}$ near the Rb *K*-edge ($\sim 15.2 \text{ keV}$). The calculations were conducted for a perfect surface ($\zeta = 1$ shown by a solid dark blue line) and a surface with a broad reflection (*e.g.* because of the non-zero mosaicity; $\zeta = 100$ shown by a dashed cyan line), where ζ represents the size of the reflected image relative to the intrinsic size of the beam.

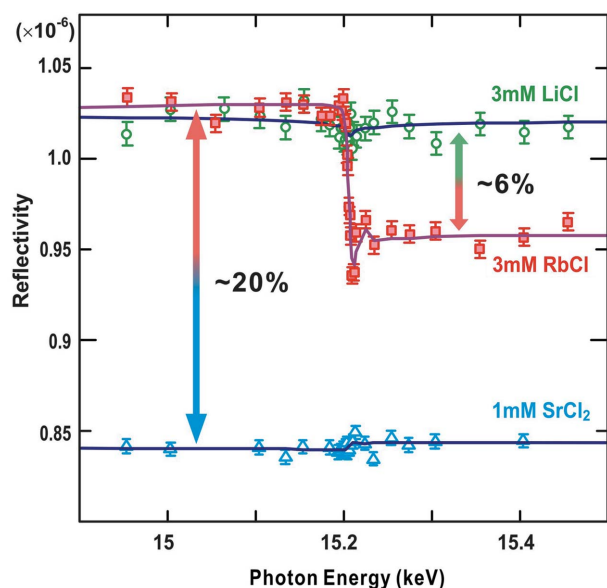


Figure 10 RAXR spectra of muscovite (001) measured using the flow-through transmission cell at $q = 0.49 \text{ \AA}^{-1}$ near the Rb *K*-edge ($\sim 15.2 \text{ keV}$), with three different solutions [3 mM LiCl (green), 3 mM RbCl (red) and 1 mM SrCl₂ (cyan)]. The data are plotted without correction for linear absorption. The solid lines through the data points are calculated based on the model-independent analyses of the data (Park & Fenter, 2007). The small modulations in the calculated lines for LiCl and SrCl₂ are mostly due to a fitting artifact. The best-fit results indicate that derived RAXR amplitudes are mostly insignificant (0.03 ± 0.02 and 0.04 ± 0.03 Rb/ A_{UC} for the LiCl and SrCl₂ data, respectively).

spectra of muscovite near the Rb *K*-edge at $q = 0.49 \text{ \AA}^{-1}$ (or $L = 1.55$ r.l.u.) are plotted for solutions of 3 mM RbCl, 3 mM LiCl and 1 mM SrCl₂ in the transmission cell. The data are plotted without correction for energy-dependent absorption by dissolved Rb, which is small for these measurements [*i.e.* $\Delta T/T(E_{Rb}) \leq 1\%$ at the Rb *K*-edge; Fig. 7(b)] compared with the RAXR signal measured in the 3 mM RbCl solution (Fig. 10). A careful choice of photon energy can substantially improve the time resolution of the measurement. The reflectivity signals for Rb- and Li-adsorbed end-members are almost identical to each other for energies below the Rb *K*-edge ($\sim 15.2 \text{ keV}$), but resonant dispersion provides a 6% contrast between these structures above the Rb *K*-edge. In contrast, the signal from the Sr-adsorbed end-member is distinct from that of the Rb-adsorbed structure both above and below the Rb *K*-edge, but with a maximum contrast of $\sim 20\%$ below the Rb *K*-edge.

3.4.2. Exchange experiments. Fig. 11 shows the measured temporal response of the reflectivity signal to several solution exchange events in the cell. Each short-dashed vertical line indicates the time at which a new solution was injected into the cell. The three solution compositions were: 3 mM RbCl (‘Rb

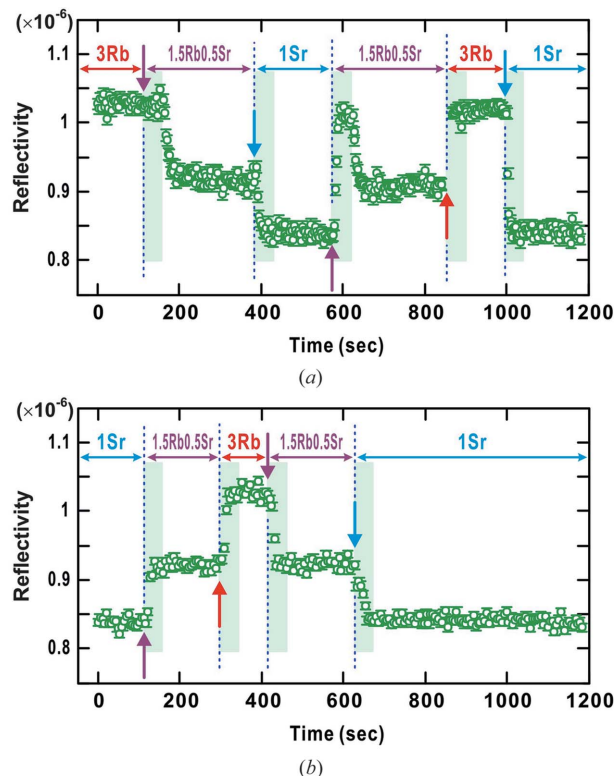


Figure 11 Sr and Rb exchange experiments at the muscovite-(001)–solution interface using a flow-through transmission cell without (Set a) and with (Set b) a mixing chamber (see §2.2 for details on the cell design). One of three solutions, 3 mM RbCl (3Rb, indicated in red), a mixture of 1.5 mM RbCl and 0.5 mM SrCl₂ (1.5Rb0.5Sr, indicated in purple), and 1 mM SrCl₂ (1Sr, indicated in cyan), was injected into the cell, initially at a fast flow rate (9 ml min^{-1}) for 40 s (indicated by the light blue band) followed by a slower flow (at 2 ml min^{-1} and 1 ml min^{-1} for Sets a and b, respectively). The time of injection for each solution is indicated with a bold arrow whose color corresponds to that of the label of the newly injected solution.

end-member'), 1 mM SrCl₂ ('Sr end-member') and 1.5 mM RbCl with 0.5 mM SrCl₂ (a 50:50 volumetric mixture of the end-member solutions). The Rb–Sr mixed solution was produced by simultaneously injecting both end-member solutions into the cell with the same flow rate (*i.e.* a half of the overall flow rate for each). The X-ray reflectivity signal was measured at $q = 0.49 \text{ \AA}^{-1}$ (or $L = 1.55 \text{ r.l.u.}$) and 15.1 keV, a photon energy below the Rb *K*-edge which maximizes the contrast between the solution conditions (Fig. 10).

Two sets of experiments were conducted. For both sets of experiments, solutions were exchanged by injecting a new solution with a fast flow rate of 9 ml min^{-1} . Given the volume of the solution chamber was 0.17 ml (the reduced cell volume is because of the sample and two Teflon cubes inserted into the cell to hold the crystal in place), full exchange of solutions (*i.e.* $\geq 99\%$) in the chamber should be achieved within $\sim 12 \text{ s}$ [equation (3)]. After 40 s at the fast rate, the rate was decreased to a rate of 2 ml min^{-1} (for 'Set a') or 1 ml min^{-1} (for 'Set b'), and maintained until the next solution exchange, using the same sequence as described above.

The 'Set a' data were collected without a mixing chamber and while injecting the solutions through an inlet on the side of the cell body. The data systematically show an unusual behavior during the fast flow period (Fig. 11*a*). The intensity was mostly unchanged from that in the Rb end-member solution even after initial injection of the Rb–Sr mixed solution. The expected change was observed after $\sim 45 \text{ s}$, corresponding to the time when the flow rate of the new solution was reduced to 2 ml min^{-1} . A more striking response was observed when the initial Sr end-member solution was exchanged with the Rb–Sr intermediate solution (at $\sim 580 \text{ s}$ in Fig. 11*a*). Here, the X-ray reflectivity signal initially increased to a level similar to that expected in the Rb end-member solution for $\sim 45 \text{ s}$ (corresponding to the fast flow period), only after which time the intensity converged to the level expected in the Rb–Sr intermediate solution. These observations indicate that the desired solution concentration at the muscovite interface was not achieved with this solution exchange scheme, especially during the initial fast exchange stage. This unusual phenomenon is presumably related to an incomplete solution mixing near the mineral surface, particularly in the high flow-rate conditions.

The 'Set b' data were collected using a solution mixing chamber (a filter membrane with a 0.45 \mu m pore size; Fig. 3) with the solution injected at the inlet at the top of the cell. The results show that the reflected intensity changed essentially immediately after injection of a new solution for all different combinations of exchanging solutions (Fig. 11*b*). These results indicate that the use of the mixing chamber as well as the change in the flow path effectively eliminates incomplete solution mixing, observed in 'Set a'.

These preliminary data (Set b, Fig. 11*b*) show that the observed intensity changes are, in general, limited by the rate of solution exchange in the cell (currently $\sim 2 \text{ s}$ for 50% solution exchange) in which the change in reflected intensity is almost instantaneous with respect to the measurement interval (2–3 s in this case). However, the temporal change in

reflected intensity appears to be resolved by the measurement during the exchange from the Rb–Sr mixture to the Sr end-member solution (near $t = 620\text{--}650 \text{ s}$), suggesting that the inherent kinetic response of the interfacial structure is slower than the other cases. We expect that ion adsorption and desorption processes at a charged mineral surface will be controlled, at least in part, by the transition between individual adsorbed species (*e.g.* inner- and outer-sphere complexes), where interfacial hydration and dehydration reactions are likely to be the rate-limiting steps. The apparently slower exchange at these conditions may be related to the difference in the sorption state between Rb⁺, which adsorbs dominantly as an inner-sphere complex, and Sr²⁺, which adsorbs as both inner- and outer-sphere complexes (Park *et al.*, 2006), and/or the change in the IS/OS fractionation of Sr in the presence and absence of a competing ion (Park *et al.*, 2008; Lee, Park *et al.*, 2010; Lee, Fenter *et al.*, 2010).

4. Discussion and summary

We demonstrate the use of a flow-through X-ray transmission cell to measure the ion adsorption thermodynamics and exchange kinetics at a mineral–solution interface and the associated technical challenges. The cell tested in this study is suitable for monitoring reactions occurring at a time scale of several seconds or longer. Additional modifications of the cell can improve the inherent rate capabilities. Reduction of the solution chamber volume can reduce the time for solution exchange in the cell. For example, a chamber with dimensions of 1 mm (v) \times 4 mm (h) \times 1 mm (length along the beam direction) to accommodate a small sample (with a surface area of 1 mm \times 4 mm, a size feasible for most mineral samples) has a volume by a factor of ~ 50 smaller than the current cell (*i.e.* 4 μl versus 0.22 ml), potentially improving the time resolution to 10 ms. The reduction of the chamber length along the beam direction, in particular, will also improve the data quality by decreasing the background intensity from solution and reducing the energy-dependent linear absorption of X-rays by the solution, which is particularly important at high ion concentrations, and enhance the cell performance at lower photon energies.

This optimized cell design will extend the applicability of high-resolution X-ray reflectivity and resonant anomalous X-ray reflectivity to studies of thermodynamics and kinetics at mineral–solution interfaces. The new cell maintains advantages of the previous generation transmission cells, having the capability of observing the spatial and temporal evolution of interfacial systems under well controlled chemical environments (*e.g.* solution composition, pH and temperature). The automated flow system adds a versatility to the cell in terms of controlling the solution composition with a high precision (*i.e.* with a $\leq 1\%$ uncertainty in mixing ratio), which will improve the accuracy of adsorption thermodynamics measurements using X-ray reflectivity, with a time resolution, potentially, of as low as $\sim 10 \text{ ms}$. The basic scheme of the cell is simple and therefore can be adapted to the specific experiment of interest

(including the shape and dimensions of the solution chamber and the cell body material). The use of this cell opens a new window through which molecular-scale reactivities can be viewed both *in situ* and in real time in various fields, including geochemistry, material sciences and environmental sciences.

This work was supported by the Geosciences Research Program, Office of Basic Energy Sciences, US Department of Energy, under Contract DE-AC02-06CH11357 to UChicago Argonne, LLC, as operator of Argonne National Laboratory. The X-ray data were collected at beamlines 6-ID-B and 33-ID-D, Advanced Photon Source. Use of the Advanced Photon Source was supported by the US Department of Energy, Office of Science, Office of Basic Energy Sciences, under Contract DE-AC02-06CH11357 to UChicago Argonne, LLC, as operator of Argonne National Laboratory. We acknowledge an anonymous reviewer for thoughtful comments.

References

- Als-Nielsen, J. & McMorrow, D. (2001). *Elements of Modern X-ray Physics*, pp. 61–106. New York: John Wiley and Sons.
- Bailey, S. W. (1984). *Micas*. Washington: The Mineralogical Society of America.
- Bellucci, F. & Nicodemo, L. (1993). *Corrosion*, **49**, 235–247.
- Bowers, G. M., Bish, D. L. & Kirkpatrick, R. J. (2008). *Langmuir*, **24**, 10240–10244.
- Brown, G. E., Henrich, V. E., Casey, W. H., Clark, D. L., Eggleston, C., Felmy, A., Goodman, D. W., Grätzel, M., Maciel, G., McCarthy, M. I., Neelson, K. H., Sverjensky, D. A., Toney, M. F. & Zachara, J. M. (1999). *Chem. Rev.* **99**, 77–174.
- Catalano, J. G., Fenter, P. & Park, C. (2009). *Geochim. Cosmochim. Acta*, **73**, 2242–2251.
- Catalano, J. G., Park, C., Fenter, P. & Zhang, Z. (2008). *Geochim. Cosmochim. Acta*, **72**, 1986–2004.
- Cheng, L., Fenter, P., Nagy, K. L., Schlegel, M. L. & Sturchio, N. C. (2001). *Phys. Rev. Lett.* **87**, 156103.
- Eng, P. J., Trainor, T. P., Brown, G. E., Waychunas, G. A., Newville, M., Sutton, S. R. & Rivers, M. L. (2000). *Science*, **288**, 1029–1033.
- Feidenhans'l, R. (1989). *Surf. Sci. Rep.* **10**, 105–188.
- Fenter, P. A. (2002). *Rev. Mineral. Geochem.* **49**, 149–220.
- Fenter, P., Catalano, J. G., Park, C. & Zhang, Z. (2006). *J. Synchrotron Rad.* **13**, 293–303.
- Fenter, P., Lee, S. S., Park, C., Catalano, J. G., Zhang, Z. & Sturchio, N. C. (2010). *Geochim. Cosmochim. Acta*, **74**, 3396–3411.
- Fenter, P., Lee, S. S., Zhang, Z. & Sturchio, N. C. (2011). *J. Appl. Phys.* **110**, 102211.
- Fenter, P., Park, C., Cheng, L., Zhang, Z., Krekeler, M. P. S. & Sturchio, N. C. (2003). *Geochim. Cosmochim. Acta*, **67**, 197–211.
- Fenter, P., Park, C. & Sturchio, N. C. (2008). *Geochim. Cosmochim. Acta*, **72**, 1848–1863.
- Fenter, P. & Sturchio, N. C. (2004). *Prog. Surf. Sci.* **77**, 171–258.
- Heberling, F., Trainor, T. P., Lützenkirchen, J., Eng, P., Denecke, M. A. & Bosbach, D. (2011). *J. Colloid Interface Sci.* **354**, 843–857.
- Israelachvili, J. N. & Pashley, R. M. (1983). *Nature (London)*, **306**, 249–250.
- Israelachvili, J. N. & Wennerström, H. (1996). *Nature (London)*, **379**, 219–225.
- Kohli, V., Bedzyk, M. J. & Fenter, P. (2010). *Phys. Rev. B*, **81**, 054112.
- Kohli, V., Zhang, Z., Park, C. & Fenter, P. (2009). *Langmuir*, **26**, 950–958.
- Lee, S. S., Fenter, P., Nagy, K. L. & Sturchio, N. C. (2012). *Langmuir*, **28**, 8637–8650.
- Lee, S. S., Fenter, P., Park, C., Sturchio, N. C. & Nagy, K. L. (2010). *Langmuir*, **26**, 16647–16651.
- Lee, S. S., Nagy, K. L. & Fenter, P. (2007). *Geochim. Cosmochim. Acta*, **71**, 5763–5781.
- Lee, S. S., Nagy, K. L., Park, C. & Fenter, P. (2009). *Environ. Sci. Technol.* **43**, 5295–5300.
- Lee, S. S., Nagy, K. L., Park, C. & Fenter, P. (2011). *Environ. Sci. Technol.* **45**, 9574–9581.
- Lee, S. S., Park, C., Fenter, P., Sturchio, N. C. & Nagy, K. L. (2010). *Geochim. Cosmochim. Acta*, **74**, 1762–1776.
- Loh, S. H. & Jarvis, S. P. (2010). *Langmuir*, **26**, 9176–9178.
- Nagy, Z. & You, H. (2002). *Electrochim. Acta*, **47**, 3037–3055.
- Park, C. & Fenter, P. A. (2007). *J. Appl. Cryst.* **40**, 290–301.
- Park, C., Fenter, P. A., Nagy, K. L. & Sturchio, N. C. (2006). *Phys. Rev. Lett.* **97**, 016101.
- Park, C., Fenter, P. A., Sturchio, N. C. & Nagy, K. L. (2008). *Langmuir*, **24**, 13993–14004.
- Park, C., Fenter, P. A., Sturchio, N. C. & Regalbuto, J. R. (2005). *Phys. Rev. Lett.* **94**, 076104.
- Park, C., Fenter, P., Zhang, Z., Cheng, L. & Sturchio, N. C. (2004). *Am. Mineral.* **89**, 1647–1654.
- Pashley, R. M. (1982). *Adv. Colloid Interface Sci.* **16**, 57–62.
- Robinson, I. K. (1986). *Phys. Rev. B Condens. Matter*, **33**, 3830–3836.
- Sacher, E. & Susko, J. R. (1979). *J. Appl. Polym. Sci.* **23**, 2355–2364.
- Schlegel, M. L., Nagy, K. L., Fenter, P., Cheng, L., Sturchio, N. C. & Jacobsen, S. D. (2006). *Geochim. Cosmochim. Acta*, **70**, 3549–3565.
- Schlegel, M. L., Nagy, K. L., Fenter, P. & Sturchio, N. C. (2002). *Geochim. Cosmochim. Acta*, **66**, 3037–3054.
- Sposito, G., Skipper, N. T., Sutton, R., Park, S., Soper, A. K. & Greathouse, J. A. (1999). *Proc. Natl Acad. Sci. USA*, **96**, 3358–3364.
- Teng, H. H., Fenter, P., Cheng, L. & Sturchio, N. C. (2001). *Geochim. Cosmochim. Acta*, **65**, 3459–3474.